
LATTE: Latent Trajectory Embedding for Diffusion-Generated Image Detection

Ana Vasilcoiu^{*1}, Ivona Najdenkoska^{*1,2}, Zeno Geradts^{1,2}, Marcel Worring¹
¹University of Amsterdam, ²Netherlands Forensic Institute (NFI)

Abstract

The rapid advancement of diffusion-based image generators has made it increasingly difficult to distinguish generated from real images. This can erode trust in digital media, making it critical to develop generalizable detectors for generated images. Recent methods leverage diffusion denoising cues, but mainly focus on single-step reconstruction errors, ignoring the inherent sequential nature of the denoising process. In this work, we propose **LATTE** - **Latent Trajectory Embedding** - a novel approach that models the evolution of latent embeddings across several denoising timesteps. By modeling the trajectory of such embeddings rather than single-step errors, LATTE captures subtle, discriminative patterns that distinguish real from generated images. Each latent is refined by employing our latent-visual feature refinement module and aggregated into a unified representation. Afterwards, it is fused with the visual features and finally passed into a lightweight classifier. Our experiments demonstrate that LATTE surpasses the baselines on several established benchmarks, such as GenImage and DiffusionFake. Moreover, it demonstrates strong performance in cross-generator and cross-datasets settings, highlighting the potential of using the trajectory of latent embeddings for generated image detection. The code is available on the following link: <https://github.com/AnaMVasilcoiu/LATTE-Diffusion-Detector>.

1 Introduction

Diffusion-based generative models have fundamentally transformed the field of image generation [1–6]. These models generate photorealistic content - such as portraits, landscapes, and complex scenes, by iteratively adding and then removing noise from data or latent representations, typically guided by a text prompt [7]. While this progress has unlocked transformative and creative applications, it has also facilitated the creation of fake images that are indistinguishable from authentic content. Such capabilities have already been exploited by malicious actors for various purposes, such as creating fraudulent impersonations of public figures [8, 9] or fabricating “evidence” in legal disputes [10–12], posing serious risks across political and social domains. These emerging threats underscore the urgent need for generated image detectors.

Recent efforts to detect diffusion-generated images [13–18] have begun to exploit the distinctive signatures left by the generative process. For example, DIRE [13] hypothesizes that diffusion models can reconstruct synthetic images more accurately than real ones. Based on this insight, they proposed a novel representation that captures the error between an input image and its reconstruction, using this signal for classification. Another work, LaRE [14] proposes a more efficient alternative by performing only a single reverse diffusion step in latent space, rather than executing the full denoising trajectory, while still producing a discriminative error-based signal. Although these recent detection methods demonstrate strong performance, they overlook the inherent sequential nature of denoising. This

^{*}Shared authorship. Correspondence to ana-maria.vasilcoiu@student.uva.nl and i.najdenkoska@uva.nl.

limitation also hampers cross-generator generalization, since single-step errors and spatial artifacts fail to capture the consistent trajectory patterns shared across different generator pipelines.

In this paper, we introduce **Latent Trajectory Embedding - LATTE**, a novel framework that explicitly models the sequential evolution of latent representations across multiple denoising steps. During generation, diffusion models produce an image through a sequence of gradual denoising steps. At each step, the model applies a learned update that iteratively refines the sample, guiding it closer to the data manifold and producing an evolving representation. This iterative process defines a trajectory that reflects how the model interprets and refines the underlying content. We hypothesize that real images - whose details and textures can lie outside the model’s learned manifold - will often produce small inconsistencies between successive denoising steps, whereas fake images will follow smoother, more self-consistent trajectories. By sampling, refining, and aggregating these latent states, LATTE captures these irregularities that enable it to distinguish real from generated images.

Specifically, given an image, we leverage a pretrained latent diffusion model to encode it into the latent space. Next, we apply forward noising and extract intermediate latent states during partial denoising at evenly spaced timesteps. We empirically find that evenly spacing the timesteps ensures coverage of early, mid, and late denoising stages, capturing the broad spectrum of the denoising dynamics. While this trajectory captures how the internal representation changes across steps, it does not indicate which image regions drive these changes. To enrich the LATTE representation, each latent is refined using a stack of transformer decoders that cross-attend to spatial features extracted from a pretrained image encoder. The refined sequence is then aggregated into a unified representation, fused with a global image feature, and passed to a lightweight classifier. This combination of latent dynamics and semantic cues enables LATTE to detect subtle inconsistencies indicative of generated content.

We evaluate LATTE on two large-scale benchmarks, namely GenImage [19] and Diffusion Forensics [13], which include fake images generated by a diverse set of diffusion models. On average, our model surpasses current state-of-the-art methods, demonstrating strong detection performance. We report an average improvement of 3.1% on GenImage and a 7.1% in cross-domain settings on Diffusion Forensics. In particular, on one of the most challenging subsets of GenImage i.e., BigGAN [20] — the only GAN-based generator - LATTE outperforms LaRE [14] by 13.3%, highlighting its cross-generator generalizability. In the cross-domain settings - for instance, the Bedroom partition of Diffusion Forensics - we observe a 16.3% gain over LaRE [14], underscoring LATTE’s ability to generalize to specialized domains.

In summary, our contributions are threefold: (1) We propose LATTE, the first diffusion-based feature that explicitly leverages the trajectory of latent states across multiple denoising steps. (2) We introduce a two-stage architecture that (i) samples and refines the latent trajectories via transformer decoders, and (ii) aggregates these refined embeddings into a compact, discriminative representation. (3) We demonstrate that LATTE achieves state-of-the-art performance and strong generalization across multiple image detection benchmarks, unseen generators, and domains.

2 Related Work

2.1 Image Generation Models

Early methods for image synthesis were predominantly based on Generative Adversarial Networks (GANs) [21, 22, 20, 23–25], Variational Autoencoders (VAEs) [26–31], and autoregressive models [32–35], each introducing foundational ideas that shaped the evolution of generative modeling. GANs produce realistic images, but are hard to train and lack stable likelihood estimation. VAEs enable efficient inference and structured latent spaces but tend to generate blurry images. Autoregressive models offer precise likelihood modeling and detail but suffer from slow, sequential sampling, especially at high resolutions.

To address earlier limitations, Denoising Diffusion Probabilistic Models (DDPMs) [1] introduced a generative process that reverses a gradual noising procedure, offering stable likelihood-based training and state-of-the-art image quality. Further advancements have explored improved sampling efficiency [2], accelerated solvers [36], architectural refinements [5, 4], and improved conditional generation with classifier-free guidance [37]. Latent Diffusion Models (LDMs) [3] improved scalability by operating in a compressed latent space learned via a variational autoencoder, enabling high-resolution synthesis at much lower cost. LDMs underpin popular models like Stable Diffusion, and have enabled

extensions such as ControlNet [38] for spatial conditioning, SDXL [6] for ultra-high-resolution output, and LCM [39] for efficient few-step sampling.

In summary, diffusion-based models combine stable, likelihood-based training with fast, high-fidelity generation and have rapidly become the dominant paradigm in image generation. Their ability to produce highly realistic text-to-image content has significantly diminished the distinction between real and generated imagery, raising growing concerns around disinformation, media manipulation, and content authenticity. As a result, diffusion models now represent the primary focus of current research in generated image detection, as also addressed in this paper.

2.2 Generated Image Detection

Early efforts in generated image detection primarily focused on GAN-generated content. Initial approaches relied on handcrafted features [40, 41], and later evolved into convolutional neural networks (CNNs) trained on large-scale datasets like FaceForensics++ [42]. Subsequent works explored more intrinsic traces of manipulation, including spectral artifacts in the frequency domain [43, 44] and inconsistencies in noise distributions [45, 46]. Although these approaches improved robustness across GANs, they have shown limited generalizability to diffusion-generated images.

In response to the unique characteristics of diffusion-based generation, recent research has proposed detection strategies that leverage the inherent internal mechanics of the diffusion process. Some approaches focus on full image reconstruction: DIRE [13] introduced the idea of using DDIM [2] inversion error as a discriminative feature, while DRCT [16] uses a contrastive training objective on reconstructed images, and FIRE [47] emphasizes mid-frequency components in reconstruction errors. Other methods extract additional signals from the reverse denoising process. LaRE [14] improves efficiency by operating in latent space and using a single-step inversion. DNF [17] and SeDID [18] both leverage the predicted noise during denoising as an indicator of authenticity. On the contrary, in this work, we leverage the trajectory of latent states across multiple denoising steps as a more robust, discriminative image representation, aware of the evolution of the denoising process.

Another line of research explores the use of powerful vision encoders, such as CLIP [48], which leverage vision-language alignment to capture rich semantic representations. These approaches use CLIP either as a frozen feature extractor with downstream classifiers [49], or in fine-tuned multi-modal frameworks that align image and text embeddings to capture inconsistencies in generated content [50, 51]. In this work, we also employ the vision encoder of CLIP in our experiments, alongside other large-scale vision encoders.

3 Methodology

In this section, we introduce our **Latent Trajectory Embedding (LATTE)** for diffusion-generated image detection. LATTE leverages the trajectory of the latent representations produced during the diffusion denoising process. In the next parts of this section, we first give a brief overview of the denoising process in latent diffusion models. Then, we continue by introducing LATTE and explaining how to extract and embed a sequence of latents into a unified trajectory representation. Finally, we explain how LATTE can be fused with visual features to enhance the detection of diffusion-generated images.

3.1 Preliminaries

Diffusion Probabilistic Models. Diffusion models define a Markov chain of diffusion steps that progressively add Gaussian noise to data until turning it into noise. In the literature, this is referred to as a forward noising process [1]. Specifically, starting from a clean image x , the forward chain gradually injects Gaussian noise over T discrete steps:

$$q(x_t | x_{t-1}) = \mathcal{N}(x_t; \sqrt{\alpha_t} x_{t-1}, (1 - \alpha_t)\mathbf{I}), \quad (1)$$

where x_t is the noisy image at step t and the schedule $\{\alpha_t\}$ controls the noise variance at each step. After T steps, the image becomes nearly isotropic noise. In the reverse process, also defined as a Markov chain, the noisy image is gradually denoised to obtain the raw image. This process leverages a neural network $\epsilon_\theta(x_t, t)$ to predict and remove this noise, defined as:

$$p_\theta(x_{t-1} | x_t) = \mathcal{N}(x_{t-1}; \frac{1}{\sqrt{\alpha_t}}(x_t - (1 - \alpha_t)\epsilon_\theta(x_t, t)), \sigma_t^2 \mathbf{I}). \quad (2)$$

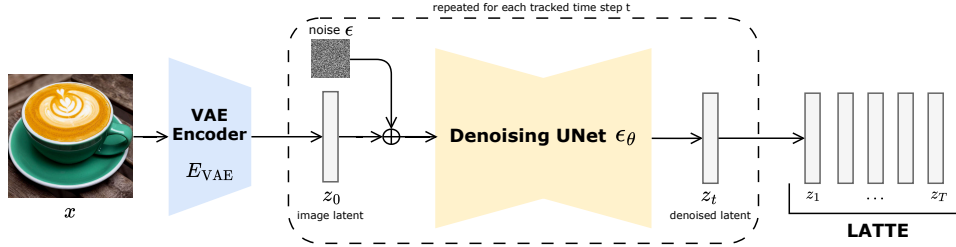


Figure 1: **Extraction of LATTE representation.** We construct the LATTE sequence by performing a single-step reconstruction for a selection of timesteps throughout the whole trajectory.

Latent Diffusion. To improve efficiency, latent diffusion models [3] first encode images into a lower-dimensional latent space via a pretrained VAE encoder E_{VAE} , producing $z_0 = E_{\text{VAE}}(x_0)$. The forward and reverse diffusion processes then operate on these latent codes $z_t \in \mathbb{R}^d$:

$$q(z_t | z_{t-1}) = \mathcal{N}(z_t; \sqrt{\alpha_t} z_{t-1}, (1 - \alpha_t)\mathbf{I}), \quad (3)$$

$$p_\theta(z_{t-1} | z_t) = \mathcal{N}(z_{t-1}; \mu_\theta(z_t, t), \Sigma_\theta(z_t, t)), \quad (4)$$

where ϵ_θ is the neural network trained to predict the noise ϵ . After denoising to z_0 , a VAE decoder D_{VAE} reconstructs the final image $\hat{x} = D_{\text{VAE}}(z_0)$. Latent diffusion thus preserves high sample quality while significantly reducing computational and memory demands.

3.2 LATTE: Latent Trajectory Embedding

Diffusion models generate images by iteratively denoising a latent variable, gradually transforming noise into structure over a sequence of timesteps. To capture this progression, we propose LATTE, a representation that reflects how the latent evolves during the generative process. Rather than performing full reverse sampling, which is computationally expensive, we leverage the denoising model’s ability to operate at any time step t and approximate the latent states with a single-step denoising per selected timestep.

Given an input image x , we first encode it into latent space using a pretrained VAE encoder: $z_0 = E_{\text{VAE}}(x)$. Next, for each selected timestep t_i , we simulate the forward diffusion process in one closed-form operation, producing a noisy latent:

$$z_t = \sqrt{\bar{\alpha}_t} z_0 + \sqrt{1 - \bar{\alpha}_t} \epsilon, \quad \epsilon \sim \mathcal{N}(0, I), \quad (5)$$

where $\bar{\alpha}_t = \prod_{s=1}^t \alpha_s$ accumulates the noise schedule up to t . We then approximate the reverse diffusion at t by performing a single denoising update using the pretrained UNet’s noise predictor ϵ_θ :

$$\hat{z}_t = z_t - \sqrt{1 - \alpha_t} \epsilon_\theta(z_t, t). \quad (6)$$

This one-step correction yields an estimate \hat{z}_t that closely approximates the latent at t , while avoiding the overhead of a full reverse pass from T to t . By repeating this forward-then-single-step reverse procedure for each of the T timesteps $\{t, \dots, T\}$ chosen to uniformly span the denoising schedule, we assemble the latent trajectory embeddings: $\mathcal{T}(x) = \{\hat{z}_1, \hat{z}_2, \dots, \hat{z}_T\}$ (see Figure 1). Crucially, this reduces latent feature extraction time by an order of magnitude compared to full reverse diffusion, as also discussed in [14].

3.3 Architecture Details

Our architecture combines two complementary feature streams — the LATTE sequence and visual semantics — to detect diffusion-generated images. As shown in Figure 2, it consists of two main stages: Latent–Visual *Feature Refinement* and Latent–Visual *Fusion & Classification*, which we describe next.

3.3.1 Latent–Visual Feature Refinement

To ground the denoising trajectory in the image content and highlight discriminative regions, each latent embedding is refined through cross-attention with spatial features extracted from a pretrained vision encoder.

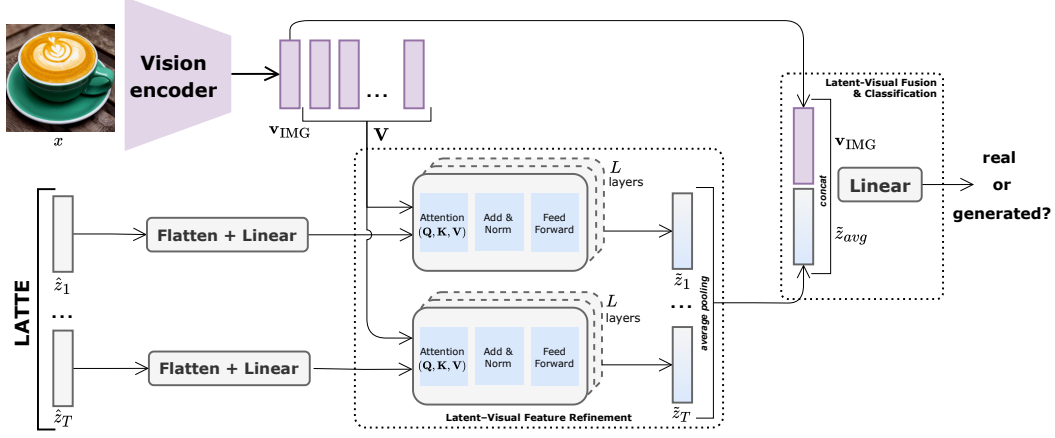


Figure 2: **Overview of our proposed architecture using LATTE.** It encompasses two main stages, namely, (1) Latent-Visual *Feature Refinement* where the LATTE is refined through stacks of L cross-attention layers and (2) Latent-Visual *Fusion & Classification* for the final fusing with the visual features and predicting the output.

Given an input image x , the encoder produces two outputs: (1) patch-level visual embeddings $V \in \mathbb{R}^{N \times d}$, and (2) a global image token $\mathbf{v}_{\text{IMG}} \in \mathbb{R}^d$. The patch tokens V capture fine-grained spatial and semantic information from the image and are leveraged for the refinement of the LATTEs. The \mathbf{v}_{IMG} token provides a holistic representation of the image and is used in the second stage.

Each latent embedding \hat{z}_t in the trajectory $\mathcal{T}(x)$ is first flattened and linearly projected to match the dimensions d of the visual features. The projected latents are then independently refined using a stack of L transformer decoders, each consisting of a cross-attention layer followed by a feed-forward layer, with residual connections and layer normalization. Specifically, each latent \hat{z}_t attends to the patch-level visual embeddings V using multi-head cross-attention (MHA) mechanism:

$$\tilde{z}_t = \text{MHA}(Q, K, V) = [\text{head}_1, \dots, \text{head}_h] \mathbf{W}^O, \text{ where } \text{head}_i = \text{softmax} \left(\frac{\hat{z}_t K^\top}{\sqrt{d}} \right) V, \quad (7)$$

where the keys and values $K, V \in \mathbb{R}^{N \times d}$ are both the visual features V , \mathbf{W}^O is the output projection layer, h is the number of heads and d is the dimension of the embeddings. Each \hat{z}_t is refined through L such layers, allowing it to align with different spatial features in the image independently of the other timesteps.

3.3.2 Latent-Visual Fusion & Classification

After refining each latent embedding through L transformer decoder layers, we obtain a set of enriched embeddings $\tilde{z}_1, \dots, \tilde{z}_T$. To aggregate this sequence into a unified representation, we perform average pooling across all T latents. Formally, we compute: $\tilde{z}_{\text{avg}} = \frac{1}{T} \sum_{i=1}^T \tilde{z}_i$.

This aggregated representation encodes how the latent embeddings transition through successive denoising steps, effectively summarizing the image’s reconstruction trajectory. Next, to incorporate a holistic semantic-level context, we concatenate \tilde{z}_{avg} with the global image token \mathbf{v}_{IMG} :

$$\mathbf{z} = [\tilde{z}_{\text{avg}} \parallel \mathbf{v}_{\text{IMG}}] \in \mathbb{R}^{2d}, \quad (8)$$

Finally, we feed this joint embedding \mathbf{z} into a lightweight linear classifier, which leverages this combined information to make a real-vs-generated prediction. By pooling refined latent embeddings and grounding them with the spatial semantics, our aggregation strategy effectively amplifies subtle artifacts that single-step or pixel-based methods tend to miss.

4 Experiments & Results

4.1 Experimental Setup

Datasets and pre-processing. We conduct our experiments on the GenImage dataset [19]², which comprises real and fake images generated by 8 different generative models: BigGAN [20], GLIDE [4], VQDM [52], Stable Diffusion V1.4 and V1.5 [7], ADM [53], Midjourney [54], and Wukong [55]. While GenImage serves as our primary benchmark, we also include the Diffusion Forensics [13]³ dataset for additional cross-generator evaluation. All images are resized to 224×224 before being passed to the model.

Evaluation metrics. Following standard practice in generated image detection, we evaluate the effectiveness of our models using accuracy (ACC) and average precision (AP). These metrics provide a comprehensive view of both overall classification performance and precision-recall trade-offs.

Training details. We extract the latent trajectories using Stable Diffusion 2.1⁴ as a denoising model. We empirically chose five evenly spaced timesteps: [981, 741, 521, 261, 1] for extracting the latents. The visual features are encoded with a pretrained ConvNeXt [56]⁵ yielding a dimension size of 512. All models are trained by minimizing binary cross-entropy loss to convergence, monitored on a held-out validation split matching the training generator. We use a batch size of 32, AdamW [57] optimizer (learning rate = $1e-4$, weight decay = $4e-5$), and a cosine-annealed learning rate scheduler. The experiments are conducted on a single H100 GPU, by training approximately 2 hours for a single epoch. The code is available at: <https://github.com/AnaMvasilcoiu/LATTE-Diffusion-Detector>.

4.2 Comparison to Baselines

We first evaluate our proposed method on GenImage [19], which is essentially testing cross-generator generalization performance. Specifically, we train our model on a given subset and test on all other subsets, and then we repeat this across all eight generators. Table 1 presents the averaged accuracy of our method in comparison to a range of existing baselines, while Figure 3 provides a complete breakdown of the results, in terms of accuracy and average precision, across all subsets. It can be observed that LATTE achieves the highest average accuracy, exceeding or matching the baselines. In particular, on one of the most challenging subsets, such as BigGAN — which is the only GAN-based generator — LATTE outperforms LaRE by 13.8%. This demonstrates that explicitly modeling trajectory evolution in the latent space yields more generalizable detection across diverse generators.

Table 1: **Accuracy(%) comparison of LATTE and other baselines on GenImage.** Each value represents the averaged accuracy across the test sets of each generator. LATTE attains top-tier average accuracy, demonstrating the potential of the latent trajectory modeling.

Method	Midjourney	SDv1.4	SDv1.5	ADM	GLIDE	Wukong	VQDM	BigGAN	Avg.
CNNSpot [58]	58.2	70.3	70.2	57.0	57.1	67.7	56.7	56.5	61.7
F3Net [59]	55.1	73.1	73.1	66.5	57.8	72.3	62.1	56.5	64.6
Spec [60]	56.7	72.4	72.3	57.9	65.4	70.3	61.7	64.3	65.1
ResNet-50 [61]	59.0	72.3	72.4	59.7	73.1	71.4	60.9	66.6	66.9
DIRE [13]	65.0	73.7	73.7	61.9	69.1	74.3	63.4	56.7	67.2
DeiT-S [62]	60.7	74.2	74.2	59.5	71.1	73.1	61.7	66.3	67.6
Swin-T [63]	61.7	76.0	76.1	61.3	76.9	75.1	65.8	69.5	70.3
LaRE [14]	66.4	87.3	87.1	66.7	81.3	85.5	84.4	74.0	79.1
LATTE	71.3	79.3	81.8	82.2	92.8	82.0	82.9	87.8	82.5

4.3 Cross-Domain Generalization

Additionally, we evaluate the cross-domain generalization ability of LATTE, and compare it to our baseline LaRE [14]. We are testing the best-performing model trained on the SDv1.4 subset of GenImage against the Diffusion Forensics dataset, introduced in [13]. For a fair comparison, we

²Licensed under CC BY-NC-SA 4.0.

³License not specified.

⁴Available under the CreativeML Open RAIL-M license: <https://huggingface.co/stabilityai/stable-diffusion-2-1>.

⁵Available via the timm library under the Apache 2.0 license: https://huggingface.co/timm/convnext_base.fb_in22k.

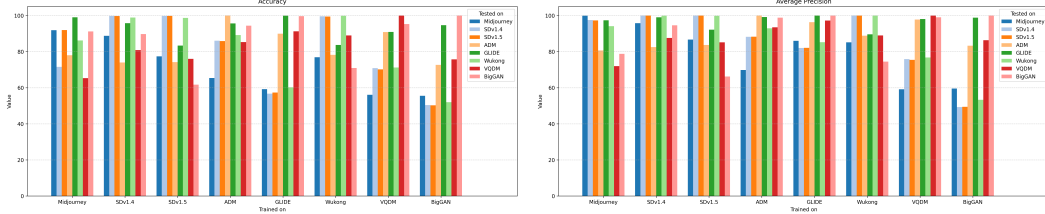


Figure 3: Accuracy(%) and average precision(%) of LATTE across the GenImage dataset. The x-axis indicates the generator used to produce the training data, while each bar represents the model’s performance when tested on data from the different generators.

retrain LaRE from scratch using the same training data as LATTE. Table 2 reports the accuracies across various generators and three distinct domains - Bedroom, ImageNet, and CelebA - which differ substantially from GenImage in both content and style, offering a robust benchmark for evaluating transferability.

Table 2: Cross-domain generalization results of models trained on GenImage and tested on Diffusion Forensics. LATTE achieves an overall average improvement of 7.1% over LaRE.

(a) Bedroom													
Method	ADM	Dalle2	DDPM	ProjGAN	StyleGAN	IDDPM	IF	LDM	MidJ	SDV	PNDM	VQDM	Avg
LaRE	53.0	66.7	57.6	50.5	62.3	55.2	90.9	93.5	90.9	78.4	53.5	82.4	69.5
LATTE	89.9	76.5	63.3	65.3	93.5	90.0	99.9	99.3	91.2	91.9	75.3	92.6	85.7

(b) ImageNet				(c) Celeba					
Method	ADM	SDV	Avg	Method	Dalle2	IF	MidJ	SDV	Avg
LaRE	81.4	98.5	89.9	LaRE	77.7	96.3	90.9	95.2	90.0
LATTE	89.8	98.0	93.9	LATTE	77.5	96.7	90.9	99.6	91.1

Our model, LATTE, consistently outperforms LaRE across all three domains, achieving improvements of 16.2% on Bedroom, 4% on Imagenet and 1.1% on Celeba, with an overall average gain of 7.1%.

4.4 Ablation Study

Influence of selected timesteps. We assess how the number of sampled timesteps n affects detection accuracy by testing four configurations. Specifically, we vary the number of denoising steps n from which intermediate latents are sampled to form the trajectory. Each configuration is denoted as T_n , where $n \in \{1, 3, 5, 9\}$. For the 5-step configuration, we chose the following steps: [981, 741, 521, 261, 1]. Given this, T1 corresponds to the single middle step ($t=521$), while T3 through T9 include both endpoints ($t=1$ and $t \approx 1000$) and interpolate additional steps evenly across the trajectory. This setup allows us to assess how increasing trajectory granularity impacts the performance. As shown in Table 3, the accuracy improves with additional timesteps up to T5, which yields the highest overall performance. Beyond this point, the T9 configuration maintains strong performance, though with slightly lower accuracy and higher processing time. These findings indicate that T5 offers the best trade-off between accuracy and efficiency. Note that the models for this ablation are trained on the Stable Diffusion v1.4 subset of GenImage.

Table 3: Accuracy(%) comparison of varying latent trajectory resolutions. We compare the effect of different timestep configurations (T_n) on the average classification accuracy across eight generative models. The best accuracy is achieved with the 5-timestep setting (T5).

Timesteps	Midjourney	SDv1.4	SDv1.5	ADM	GLIDE	Wukong	VQDM	BigGAN	Avg.
T1	80.4	99.2	98.8	71.2	85.6	96.9	74.2	62.5	83.6
T3	78.7	99.3	99.0	75.3	81.8	97.2	80.4	68.0	85.0
T5	88.7	99.8	99.7	74	95.7	98.9	80.8	89.7	90.9
T9	86.2	99.5	99.4	75.2	94.4	98.0	79.8	86.9	89.9

Influence of vision backbone choice. We examine the impact of the vision backbone on performance. Standard CLIP encoders (RN50, ViT-B/32) underperformed on GenImage in preliminary experiments, prompting the shift to higher-capacity backbones: ConvNeXt-Base pretrained on ImageNet-22k and CLIP ViT-L/14 ⁶, the latter inspired by UnivFD [64]. Both improved the results significantly, with ConvNeXt consistently achieving the highest accuracy, as demonstrated in Table 4.

Table 4: **Accuracy(%) comparison between different vision backbones.** ConvNeXt outperforms CLIP ViT-L/14 by 5.2%.

Vision encoder	Midjourney	SDv1.4	SDv1.5	ADM	GLIDE	Wukong	VQDM	BigGAN	Avg.
CLIP ViT-L/14	98.2	100	100	68.4	91.8	99.9	58.9	68.4	85.7
ConvNeXt	88.7	99.8	99.7	74.0	95.7	98.9	80.8	89.7	90.9

Benefit of average pooling strategy. The standard average pooling used to summarize timestep-specific representations assumes equal importance across all timesteps in the trajectory. To challenge this assumption, we experiment with a learned weighted pooling mechanisms that assigns importance scores to each timestep using a linear gating function and softmax normalization. While this allows different timesteps to have varying influence on the final representation, it performs worse than simple average pooling - suggesting that, in practice, all steps contribute equally informative signals.

In addition, we consider aggregation through CLS pooling. Namely, we replace the average pooling with a self-attention over the sequence of refined latents with added positional encodings. We prepend a [CLS] token that serves as the trajectory aggregation. The goal is to assess whether allowing latents to refine each other via self-attention and incorporate sequence order can improve performance. However, this variant underperforms compared to simple average pooling, suggesting that the refined LATTE is already expressive enough without additional self-attention refinements, as seen in Table 5.

Table 5: **Accuracy(%) comparison between different aggregation strategies.** Average pooling outperforms learnable weighted pooling by 9.3% and CLS pooling by 1.3%.

Configuration	Midjourney	SDv1.4	SDv1.5	ADM	GLIDE	Wukong	VQDM	BigGAN	Avg.
Weighted pooling	73.0	99.8	99.7	72.0	79.0	98.7	74.4	56.3	81.6
CLS pooling	85.8	99.0	99.0	83.2	86.7	96.8	88.7	77.8	89.6
Average pooling	88.7	99.8	99.7	74.0	95.7	98.9	80.8	89.7	90.9

4.5 Embedding Space Analysis

Besides quantitative results, we assess our model’s discriminative capacity by visualizing real and generated image embeddings with t-SNE [65]. The first row of Figure 4 depicts the embeddings extracted from the original, frozen ConvNeXt backbone, while the second row displays embeddings after the backbone has been fine-tuned during LATTE training.

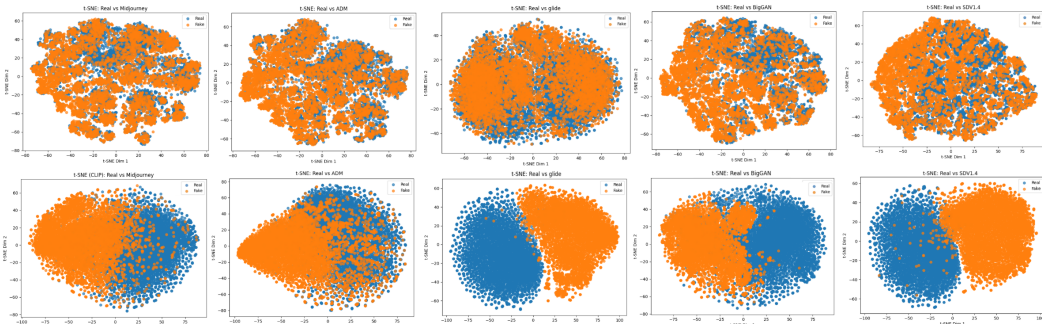


Figure 4: **Visualizations of t-SNE embeddings for real and fake images across five generators from GenImage.** The first row presents embeddings before using LATTE (extracted using the original ConvNeXt), while the second row shows embeddings derived from LATTE. The reduced overlap in the second row indicates LATTE’s discriminative power and generalization capabilities.

⁶Available under the MIT License: <https://github.com/openai/CLIP>.

The embeddings in the second row exhibit much clearer separation between real (blue) and fake (orange) samples, indicating reduced overlap and stronger class separation. This clear separation demonstrates that LATTE’s joint training captures the latent trajectory dynamics and adapts the visual encoder to better distinguish generated content.

4.6 Robustness to Perturbations

Additionally, we assess the robustness of LATTE under common post-processing operations like compression, resizing, Gaussian blur, and Gaussian noise. Such perturbations often occur in real-world pipelines and can severely degrade the subtle artifacts that detection methods depend on. As shown in Figure 5, LATTE consistently outperforms LaRE, maintaining higher detection accuracy and greater stability. This shows that LATTE’s reliance on multi-step latent trajectories is more invariant under such transformations than single-step reconstruction errors.

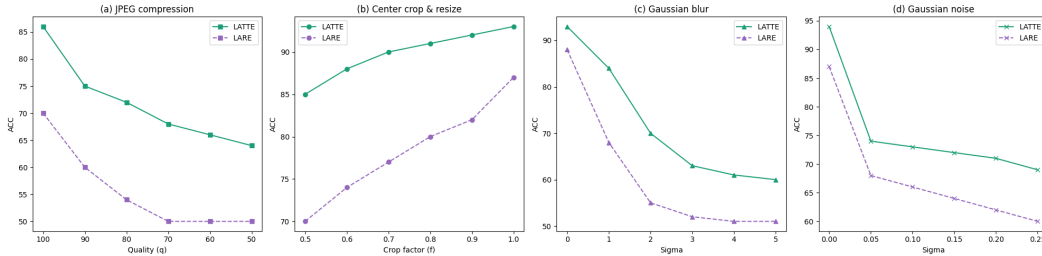


Figure 5: **Accuracy (%) of LATTE and LaRE on perturbed images.** We evaluate and compare the robustness of both methods under four common post-processing transformations: JPEG compression, Center crop & resize, Gaussian blur, and noise. LATTE consistently outperforms LaRE across all considered perturbations.

4.7 Qualitative Analysis

To complement the quantitative results, we present a selection of qualitative examples in Figure 6, organized in a confusion-matrix-style layout. This visualization provides insight into typical model successes and failure cases, illustrating the visual characteristics that influence detection outcomes and highlighting both the strengths and limitations of the proposed approach.

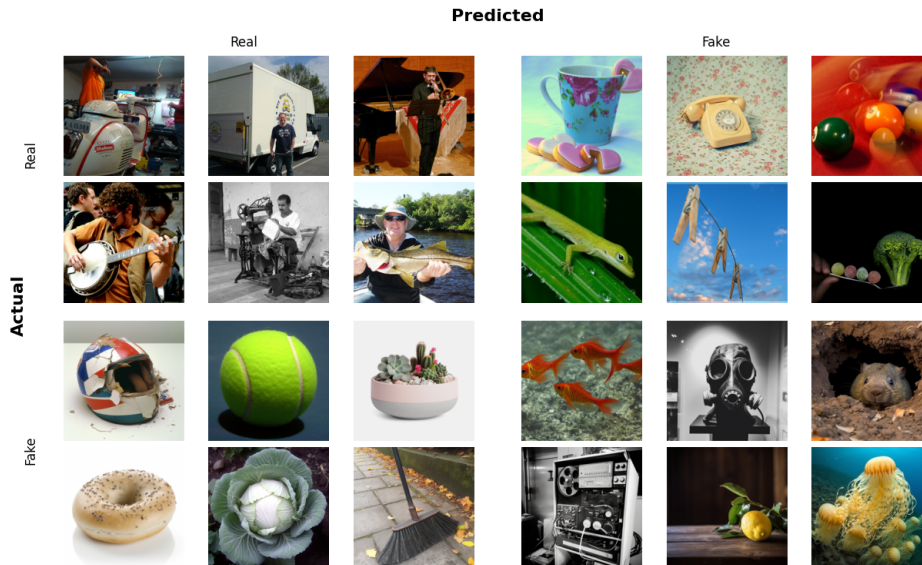


Figure 6: **Qualitative results in a confusion-matrix-style layout.** The rows show actual labels, and the columns show predictions of LATTE.

Top-left: True negatives. This quadrant displays real images that the model correctly identifies as real. These examples contain complex textures, human subjects, or high-frequency structural details. Such content remains inherently difficult for generative models to replicate with full fidelity, resulting in strong detection cues. This observation reflects a broader trend across the GenImage dataset, namely that real-world images characterized by organic structure, intricate details, or recognizable human elements are consistently classified correctly, highlighting the model’s strength in identifying authentic content.

Top-right: False Positives. These are real images that the model mistakenly classifies as fake. A common pattern among these examples is the presence of smooth textures, highly saturated colors, or stylized lighting, visual characteristics often associated with generative outputs. Real images that stylistically resemble synthetic content, such as those with artistic post-processing, exaggerated lighting, or minimal texture complexity, tend to trigger false alarms. This reflects a known limitation, where the model may overestimate the likelihood of manipulation in real images that exhibit generative-like visual properties.

Bottom-left: False Negatives. This quadrant contains generated images that the model fails to detect, incorrectly classifying them as real. Many of these examples depict simple objects, clean compositions, or scenes lacking complex structure or obvious artifacts. When generated content exhibits high visual plausibility and avoids common generative flaws, the model’s detection performance degrades. Such borderline cases, where fakes are indistinguishable from real content, particularly when lacking intricate textures or irregularities, remain a challenge for our latent trajectory-based detection method. These examples underscore the difficulty of reliably identifying high-quality synthetic images and highlight the growing need for robust, adaptive detectors, especially in light of the rapid advancements in generative model capabilities.

Bottom-right: True Positives. These are generated images correctly identified as fake by the model. Despite appearing visually convincing at first glance, the subtle generative traces embedded in the latent denoising trajectory leveraged by LATTE enable reliable detection. Our detector does not rely on superficial visual artifacts but instead exploits inconsistencies inherent to the generative process, often imperceptible to humans. While high-quality synthetic images remain a significant challenge for detection methods, as highlighted in the previous quadrant, these examples illustrate that LATTE takes an important step toward overcoming this difficulty, enabling reliable identification even for visually plausible, high-fidelity fakes.

5 Conclusion

We introduced LATTE, the first approach to explicitly model the trajectory of latent embeddings across diffusion denoising steps. Our two-stage architecture - (i) Latent-Visual Feature Refinement and (ii) Latent-Visual Fusion & Classification - yields performance gains over prior work and improved generalization capabilities. In particular, LATTE achieves an average accuracy of 82.2% on the GenImage dataset (a 3.1% improvement over LaRE), and delivers a 7.1% gain in cross-domain accuracy on Diffusion Forensics, underscoring the effectiveness of leveraging latent trajectory dynamics for robust generated-image detection. We believe these findings pave the way for future research into latent trajectory-aware detection features for generalizable generated image detection.

Limitations. While LATTE achieves strong performance and improved generalization, its effectiveness diminishes under strong post-processing (e.g., heavy JPEG compression or strong blur), indicating sensitivity to distribution shifts. Additionally, like most global detectors, LATTE has been evaluated primarily on fully synthetic versus real images. Detecting small, localized forgeries is a different task and remains an open challenge for future work.

Broader Impact. Our work contributes to the detection of diffusion-generated images, supporting efforts to counter disinformation and enhance media authenticity. However, as with any detection method, it may prompt adversarial adaptation or be misused in contexts where real content is unjustly flagged. Future work should consider robust evaluation in real-world situations and mitigation strategies for misuse.

References

- [1] Jonathan Ho, Ajay Jain, and Pieter Abbeel. Denoising diffusion probabilistic models. *Advances in neural information processing systems*, 33:6840–6851, 2020.
- [2] Jiaming Song, Chenlin Meng, and Stefano Ermon. Denoising diffusion implicit models. *arXiv preprint arXiv:2010.02502*, 2020.
- [3] Robin Rombach, Andreas Blattmann, Dominik Lorenz, Patrick Esser, and Björn Ommer. High-resolution image synthesis with latent diffusion models. In *Proceedings of the IEEE/CVF conference on computer vision and pattern recognition*, pages 10684–10695, 2022.
- [4] Alex Nichol, Prafulla Dhariwal, Aditya Ramesh, Pranav Shyam, Pamela Mishkin, Bob McGrew, Ilya Sutskever, and Mark Chen. Glide: Towards photorealistic image generation and editing with text-guided diffusion models. *arXiv preprint arXiv:2112.10741*, 2021.
- [5] Chitwan Saharia, William Chan, Saurabh Saxena, Lala Li, Jay Whang, Emily L Denton, Kamyar Ghasemipour, Raphael Gontijo Lopes, Burcu Karagol Ayan, Tim Salimans, et al. Photorealistic text-to-image diffusion models with deep language understanding. *Advances in neural information processing systems*, 35:36479–36494, 2022.
- [6] Dustin Podell, Zion English, Kyle Lacey, Andreas Blattmann, Tim Dockhorn, Jonas Müller, Joe Penna, and Robin Rombach. Sdxl: Improving latent diffusion models for high-resolution image synthesis. *arXiv preprint arXiv:2307.01952*, 2023.
- [7] Robin Rombach, Andreas Blattmann, Dominik Lorenz, Patrick Esser, and Björn Ommer. High-resolution image synthesis with latent diffusion models. In *Proceedings of the IEEE/CVF conference on computer vision and pattern recognition*, pages 10684–10695, 2022.
- [8] John Twomey, Didier Ching, Matthew Peter Aylett, Michael Quayle, Conor Linehan, and Gillian Murphy. Do deepfake videos undermine our epistemic trust? a thematic analysis of tweets that discuss deepfakes in the russian invasion of ukraine. *Plos one*, 18(10):e0291668, 2023.
- [9] Audrey de Rancourt-Raymond and Nadia Smaili. The unethical use of deepfakes. *Journal of Financial Crime*, 30(4):1066–1077, 2023.
- [10] Rebecca A Delfino. Deepfakes on trial: a call to expand the trial judge’s gatekeeping role to protect legal proceedings from technological fakery. *Hastings LJ*, 74:293, 2022.
- [11] Maria-Paz Sandoval, Maria de Almeida Vau, John Solaas, and Luano Rodrigues. Threat of deepfakes to the criminal justice system: a systematic review. *Crime Science*, 13(1):41, 2024.
- [12] N. Koutras and N. Selvadurai, editors. *Recreating Creativity, Reinventing Inventiveness: AI and Intellectual Property Law*. Routledge, 1st edition, 2024. doi: 10.4324/9781003260127. URL <https://doi.org/10.4324/9781003260127>.
- [13] Zhendong Wang, Jianmin Bao, Wengang Zhou, Weilun Wang, Hezhen Hu, Hong Chen, and Houqiang Li. Dire for diffusion-generated image detection. In *Proceedings of the IEEE/CVF International Conference on Computer Vision*, pages 22445–22455, 2023.
- [14] Yunpeng Luo, Junlong Du, Ke Yan, and Shouhong Ding. Lare²: Latent reconstruction error based method for diffusion-generated image detection. In *Proceedings of the IEEE/CVF Conference on Computer Vision and Pattern Recognition*, pages 17006–17015, 2024.
- [15] Jonas Ricker, Denis Lukovnikov, and Asja Fischer. Aeroblade: Training-free detection of latent diffusion images using autoencoder reconstruction error. In *Proceedings of the IEEE/CVF Conference on Computer Vision and Pattern Recognition*, pages 9130–9140, 2024.
- [16] Baoying Chen, Jishen Zeng, Jianquan Yang, and Rui Yang. Drct: Diffusion reconstruction contrastive training towards universal detection of diffusion generated images. In *Forty-first International Conference on Machine Learning*, 2024.
- [17] Yichi Zhang and Xiaogang Xu. Diffusion noise feature: Accurate and fast generated image detection. *arXiv preprint arXiv:2312.02625*, 2023.

- [18] Ruipeng Ma, Jinhao Duan, Fei Kong, Xiaoshuang Shi, and Kaidi Xu. Exposing the fake: Effective diffusion-generated images detection. *arXiv preprint arXiv:2307.06272*, 2023.
- [19] Mingjian Zhu, Hanting Chen, Qiangyu Yan, Xudong Huang, Guanyu Lin, Wei Li, Zhijun Tu, Hailin Hu, Jie Hu, and Yunhe Wang. Genimage: A million-scale benchmark for detecting ai-generated image. *Advances in Neural Information Processing Systems*, 36:77771–77782, 2023.
- [20] Andrew Brock, Jeff Donahue, and Karen Simonyan. Large scale gan training for high fidelity natural image synthesis. *arXiv preprint arXiv:1809.11096*, 2018.
- [21] Ian Goodfellow, Jean Pouget-Abadie, Mehdi Mirza, Bing Xu, David Warde-Farley, Sherjil Ozair, Aaron Courville, and Yoshua Bengio. Generative adversarial networks. *Communications of the ACM*, 63(11):139–144, 2020.
- [22] Tero Karras, Timo Aila, Samuli Laine, and Jaakko Lehtinen. Progressive growing of gans for improved quality, stability, and variation. *arXiv preprint arXiv:1710.10196*, 2017.
- [23] Yunje Choi, Minje Choi, Munyoung Kim, Jung-Woo Ha, Sunghun Kim, and Jaegul Choo. Stargan: Unified generative adversarial networks for multi-domain image-to-image translation. In *Proceedings of the IEEE conference on computer vision and pattern recognition*, pages 8789–8797, 2018.
- [24] Taesung Park, Ming-Yu Liu, Ting-Chun Wang, and Jun-Yan Zhu. Semantic image synthesis with spatially-adaptive normalization. In *Proceedings of the IEEE/CVF conference on computer vision and pattern recognition*, pages 2337–2346, 2019.
- [25] Jun-Yan Zhu, Taesung Park, Phillip Isola, and Alexei A Efros. Unpaired image-to-image translation using cycle-consistent adversarial networks. In *Proceedings of the IEEE international conference on computer vision*, pages 2223–2232, 2017.
- [26] Diederik P Kingma, Max Welling, et al. Auto-encoding variational bayes, 2013.
- [27] Kihyuk Sohn, Honglak Lee, and Xinchen Yan. Learning structured output representation using deep conditional generative models. *Advances in neural information processing systems*, 28, 2015.
- [28] Irina Higgins, Loic Matthey, Arka Pal, Christopher Burgess, Xavier Glorot, Matthew Botvinick, Shakir Mohamed, and Alexander Lerchner. beta-vae: Learning basic visual concepts with a constrained variational framework. In *International conference on learning representations*, 2017.
- [29] Xianxu Hou, Linlin Shen, Ke Sun, and Guoping Qiu. Deep feature consistent variational autoencoder. In *2017 IEEE winter conference on applications of computer vision (WACV)*, pages 1133–1141. IEEE, 2017.
- [30] Shengjia Zhao, Jiaming Song, and Stefano Ermon. Infovae: Information maximizing variational autoencoders. *arXiv preprint arXiv:1706.02262*, 2017.
- [31] Aaron Van Den Oord, Oriol Vinyals, et al. Neural discrete representation learning. *Advances in neural information processing systems*, 30, 2017.
- [32] Aaron Van den Oord, Nal Kalchbrenner, Lasse Espeholt, Oriol Vinyals, Alex Graves, et al. Conditional image generation with pixelcnn decoders. *Advances in neural information processing systems*, 29, 2016.
- [33] Niki Parmar, Ashish Vaswani, Jakob Uszkoreit, Lukasz Kaiser, Noam Shazeer, Alexander Ku, and Dustin Tran. Image transformer. In *International conference on machine learning*, pages 4055–4064. PMLR, 2018.
- [34] Patrick Esser, Robin Rombach, and Bjorn Ommer. Taming transformers for high-resolution image synthesis. In *Proceedings of the IEEE/CVF conference on computer vision and pattern recognition*, pages 12873–12883, 2021.

- [35] Aditya Ramesh, Mikhail Pavlov, Gabriel Goh, Scott Gray, Chelsea Voss, Alec Radford, Mark Chen, and Ilya Sutskever. Zero-shot text-to-image generation. In *International conference on machine learning*, pages 8821–8831. Pmlr, 2021.
- [36] Tero Karras, Miika Aittala, Timo Aila, and Samuli Laine. Elucidating the design space of diffusion-based generative models. *Advances in neural information processing systems*, 35: 26565–26577, 2022.
- [37] Jonathan Ho and Tim Salimans. Classifier-free diffusion guidance. *arXiv preprint arXiv:2207.12598*, 2022.
- [38] Lvmin Zhang, Anyi Rao, and Maneesh Agrawala. Adding conditional control to text-to-image diffusion models. In *Proceedings of the IEEE/CVF international conference on computer vision*, pages 3836–3847, 2023.
- [39] Simian Luo, Yiqin Tan, Longbo Huang, Jian Li, and Hang Zhao. Latent consistency models: Synthesizing high-resolution images with few-step inference. *arXiv preprint arXiv:2310.04378*, 2023.
- [40] Xin Yang, Yuezun Li, and Siwei Lyu. Exposing deep fakes using inconsistent head poses. In *ICASSP 2019-2019 IEEE international conference on acoustics, speech and signal processing (ICASSP)*, pages 8261–8265. IEEE, 2019.
- [41] Chang M Liy and LYUS InIctuOculi. Exposing ai created fake videos by detecting eye blinking. In *2018 IEEE InterG national Workshop on Information Forensics and Security (WIFS)*. IEEE, 2018.
- [42] Andreas Rossler, Davide Cozzolino, Luisa Verdoliva, Christian Riess, Justus Thies, and Matthias Nießner. Faceforensics++: Learning to detect manipulated facial images. In *Proceedings of the IEEE/CVF international conference on computer vision*, pages 1–11, 2019.
- [43] Yuchen Luo, Yong Zhang, Junchi Yan, and Wei Liu. Generalizing face forgery detection with high-frequency features. In *Proceedings of the IEEE/CVF conference on computer vision and pattern recognition*, pages 16317–16326, 2021.
- [44] Joel Frank, Thorsten Eisenhofer, Lea Schönherr, Asja Fischer, Dorothea Kolossa, and Thorsten Holz. Leveraging frequency analysis for deep fake image recognition. In *International conference on machine learning*, pages 3247–3258. PMLR, 2020.
- [45] Tianyi Wang and Kam Pui Chow. Noise based deepfake detection via multi-head relative-interaction. In *Proceedings of the AAAI Conference on Artificial Intelligence*, volume 37, pages 14548–14556, 2023.
- [46] Weiming Bai, Yufan Liu, Zhipeng Zhang, Xinyi Zhang, Bo Wang, Chengwei Peng, Weiming Hu, and Bing Li. Learn from noise: Detecting deepfakes via regional noise consistency. In *2024 International Joint Conference on Neural Networks (IJCNN)*, pages 1–8. IEEE, 2024.
- [47] Beilin Chu, Xuan Xu, Xin Wang, Yufei Zhang, Weike You, and Linna Zhou. Fire: Robust detection of diffusion-generated images via frequency-guided reconstruction error. *arXiv preprint arXiv:2412.07140*, 2024.
- [48] Alec Radford, Jong Wook Kim, Chris Hallacy, Aditya Ramesh, Gabriel Goh, Sandhini Agarwal, Girish Sastry, Amanda Askell, Pamela Mishkin, Jack Clark, et al. Learning transferable visual models from natural language supervision. In *International conference on machine learning*, pages 8748–8763. PmLR, 2021.
- [49] Yaning Zhang, Tianyi Wang, Zitong Yu, Zan Gao, Linlin Shen, and Shengyong Chen. Mfclip: Multi-modal fine-grained clip for generalizable diffusion face forgery detection. *arXiv preprint arXiv:2409.09724*, 2024.
- [50] Davide Cozzolino, Giovanni Poggi, Riccardo Corvi, Matthias Nießner, and Luisa Verdoliva. Raising the bar of ai-generated image detection with clip. In *Proceedings of the IEEE/CVF Conference on Computer Vision and Pattern Recognition*, pages 4356–4366, 2024.

- [51] Dong Li, Jiaying Zhu, Xueyang Fu, Xun Guo, Yidi Liu, Gang Yang, Jiawei Liu, and Zheng-Jun Zha. Noise-assisted prompt learning for image forgery detection and localization. In *European Conference on Computer Vision*, pages 18–36. Springer, 2024.
- [52] Shuyang Gu, Dong Chen, Jianmin Bao, Fang Wen, Bo Zhang, Dongdong Chen, Lu Yuan, and Baining Guo. Vector quantized diffusion model for text-to-image synthesis. In *Proceedings of the IEEE/CVF conference on computer vision and pattern recognition*, pages 10696–10706, 2022.
- [53] Prafulla Dhariwal and Alexander Nichol. Diffusion models beat gans on image synthesis. *Advances in neural information processing systems*, 34:8780–8794, 2021.
- [54] Midjourney, 2024. URL <https://www.midjourney.com/home>.
- [55] Wukong, 2024. URL <https://xihe.mindspore.cn/modelzoo>.
- [56] Zhuang Liu, Hanzi Mao, Chao-Yuan Wu, Christoph Feichtenhofer, Trevor Darrell, and Saining Xie. A convnet for the 2020s. In *Proceedings of the IEEE/CVF conference on computer vision and pattern recognition*, pages 11976–11986, 2022.
- [57] Ilya Loshchilov and Frank Hutter. Decoupled weight decay regularization. *International Conference on Learning Representations*, 2017.
- [58] Sheng-Yu Wang, Oliver Wang, Richard Zhang, Andrew Owens, and Alexei A Efros. Cnn-generated images are surprisingly easy to spot... for now. In *Proceedings of the IEEE/CVF conference on computer vision and pattern recognition*, pages 8695–8704, 2020.
- [59] Yuyang Qian, Guojun Yin, Lu Sheng, Zixuan Chen, and Jing Shao. Thinking in frequency: Face forgery detection by mining frequency-aware clues. In *European conference on computer vision*, pages 86–103. Springer, 2020.
- [60] Xu Zhang, Svebor Karaman, and Shih-Fu Chang. Detecting and simulating artifacts in gan fake images. In *2019 IEEE international workshop on information forensics and security (WIFS)*, pages 1–6. IEEE, 2019.
- [61] Kaiming He, Xiangyu Zhang, Shaoqing Ren, and Jian Sun. Deep residual learning for image recognition. In *Proceedings of the IEEE conference on computer vision and pattern recognition*, pages 770–778, 2016.
- [62] Hugo Touvron, Matthieu Cord, Matthijs Douze, Francisco Massa, Alexandre Sablayrolles, and Hervé Jégou. Training data-efficient image transformers & distillation through attention. In *International conference on machine learning*, pages 10347–10357. PMLR, 2021.
- [63] Ze Liu, Yutong Lin, Yue Cao, Han Hu, Yixuan Wei, Zheng Zhang, Stephen Lin, and Baining Guo. Swin transformer: Hierarchical vision transformer using shifted windows. In *Proceedings of the IEEE/CVF international conference on computer vision*, pages 10012–10022, 2021.
- [64] Utkarsh Ojha, Yuheng Li, and Yong Jae Lee. Towards universal fake image detectors that generalize across generative models. In *Proceedings of the IEEE/CVF Conference on Computer Vision and Pattern Recognition*, pages 24480–24489, 2023.
- [65] Laurens van der Maaten and Geoffrey Hinton. Visualizing data using t-sne. *Journal of Machine Learning Research*, 9(86):2579–2605, 2008. URL <http://jmlr.org/papers/v9/vandermaaten08a.html>.

Supplementary material

A Complete in-domain and cross-model comparison to the baselines

In this section, we report a comprehensive matrix of pairwise detection results to complement the summary metrics in the main paper. For **DIRE** [13] and **LaRE** [14], we copy the results reported in the LaRE paper. For our method, **LATTE**, we evaluate it under the same experimental protocol to enable fair comparison. In each case, the detector is trained on images generated by one model and tested on held-out images from eight generators, producing an 8×8 matrix. Diagonal entries reflect in-domain performance (i.e. training and testing on the same generator), while off-diagonal entries measure cross-model generalization.

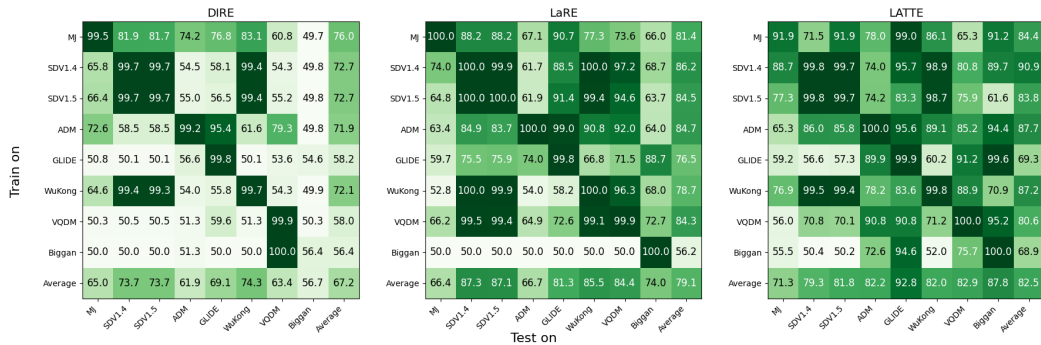


Figure 7: **Complete pairwise evaluation of detection performance** across all 8 generators in the GenImage dataset. Each subplot corresponds to one detector - DIRE (left; baseline), LaRE (center; baseline), and LATTE (right; proposed) - and shows the accuracy(%) when training on the subset listed on the vertical axis and testing on the subset listed along the horizontal axis. Row- and column-averages summarize each method’s cross-model generalization capabilities.

DIRE achieves a strong in-domain average accuracy of 94.24%, but its cross-model generalization is limited, with an off-diagonal mean of only 63.5%. LaRE substantially improves both metrics - reaching 99.96% in-domain and 76.08% off-diagonal. Our method, LATTE, maintains competitive in-domain performance at 98.89% while further boosting transfer - with an average cross-model accuracy of 80.18%, outperforming LaRE by nearly 4 percentage points. This demonstrates that incorporating temporal trajectory consistency not only preserves high fidelity on known generators but also yields the most robust detection on unseen models.

B Additional ablation studies

To further understand the key design choices and components of the LATTE framework, we conduct a series of additional ablation studies. These experiments are aimed at isolating and quantifying the contributions of individual architectural modules, processing strategies, and training configurations. All ablation results reported in this section are based on models trained using the SDv1.4 subset of the GenImage dataset. We focus on this subset since using a fixed generator allows us to isolate the effects of individual design choices without confounding variability, and SDv1.4 is a commonly used baseline in prior work (e.g. [16]), making our results easier to contextualize.

B.1 Importance of each component in LATTE

We perform an ablation study focusing on three key elements: the **visual feature** v_{IMG} from the backbone, the **latent trajectory** derived from intermediate diffusion steps, and the **Latent-Visual Feature Refinement** module that aligns and integrates these modalities via cross-attention.

We evaluate four model variants with different combinations of these components. The first baseline (A) uses visual features only, while the second (B) uses only the latent trajectory, aggregated with mean pooling. The third (C) combines the visual features with the latent trajectory, allowing the

model to capture generative dynamics, but without any refinement. The final variant (D) includes all three components.

Table 6: **Ablation on visual and latent components.** ✓ indicates the component is included. Results are shown as Accuracy (%) for each generator. Including all components outperform the visual and latent-only configurations by 16% and 37.7%.

Model	Visual	Latent	Refine	MJ	SDV1.4	SDV1.5	ADM	GLIDE	Wukong	VQDM	BigGAN	Avg.
A	✓	✗	✗	83.5	99.9	99.9	51.7	56.2	99.9	58.4	50.0	74.9
B	✗	✓	✗	50.0	58.3	58.4	50.0	50.0	56.6	52.6	50.0	53.2
C	✓	✓	✗	80.5	100	99.9	76.7	84.3	99.8	69.2	75.8	85.7
D	✓	✓	✓	88.7	99.8	99.7	74.0	95.7	98.9	80.8	89.7	90.9

As shown in Table 6, we observe that both visual-only (A) and latent-only (B) models yield relatively poor performance, indicating that neither visual semantics nor latent diffusion signals alone are sufficient for robust detection. Adding latent trajectory features to the visual backbone (C) leads to improvements across most generators, suggesting that these two modalities offer complementary cues. However, the accuracy gains are still limited, likely due to misalignment between the latent and visual representations when no refinement is applied. The full model (D), which incorporates both latent trajectories and the Latent-Visual Feature Refinement module, achieves the highest accuracy across nearly all subsets. Notably it outperforms other variants by a large margin on challenging generators (e.g. +11.6% on VQDM, +13.9% on BigGAN). These results highlight the critical role of refinement in effectively fusing latent and visual information.

B.2 Influence of separate latent processing strategy

The default LATTE architecture, as described in Section 3, processes the latent trajectory by refining each timestep independently using a dedicated transformer decoder. An alternative approach is to stack the latent embeddings from all timesteps into a single sequence and process them jointly through a shared transformer decoder stack, enforcing full parameter sharing across the sequence. As shown in Table 7, decoding each timestep separately achieves higher accuracy across most generators, suggesting that preserving per-timestep decoding helps the model retain specific features from the denoising trajectory.

Table 7: **Accuracy(%) comparison** between separate vs. joint latent processing strategies. Processing timesteps separately yields the highest average accuracy, outperforming joint processing by 0.7%.

Latent strategy	Midjourney	SDv1.4	SDv1.5	ADM	GLIDE	Wukong	VQDM	BigGAN	Avg.
Joint	88.4	99.7	99.6	72.5	94.4	98.6	79.4	88.9	90.2
Separate	88.7	99.8	99.7	74.0	95.7	98.9	80.8	89.7	90.9

B.3 Effect of position encoding in CLS-pooling

Section 4 of the paper ablates the aggregation mode by considering a CLS-style pooling variant. Specifically, we leverage a self-attention mechanism over the sequence of latents, using a prepended learnable [CLS] token. The configuration evaluated in the main results includes learnable positional embeddings to provide the model with information about the order of latents along the trajectory. Here, we conduct a focused ablation to isolate the effect of the positional embeddings. Specifically, we compare the full model (“CLS-pooling w/ pos. enc.”) to a variant that uses the same CLS-based self-attention but omits positional embeddings (“CLS-pooling w/o pos. enc.”), removing any explicit indication of timestep order. As shown in Table 8, providing sequence order information results in a significant improvement of 7.2% in average accuracy, confirming that timestep position is an important signal when aggregating latents jointly. Despite this gain, both CLS-based variants remain less effective than the default LATTE architecture, which processes each timestep independently and aggregates the outputs via average pooling. Interestingly, the “CLS-pooling w/ pos. enc.” variant demonstrates better performance on certain subsets - 9.2% increase on ADM and 7.9% on VQDM - suggesting that this CLS-based design, paired with sequence order cues can be beneficial in specific contexts. However, on average, the baseline approach still outperforms both CLS-pooling variants, highlighting that preserving timestep-specific specialization is ultimately more effective.

Table 8: **Accuracy(%) comparison** between models with and without explicit sequence order. Explicit positional embeddings improve accuracy by 7.2% over the implicit variant, but still fall short of the baseline strategy.

Sequence order	Midjourney	SDv1.4	SDv1.5	ADM	GLIDE	Wukong	VQDM	BigGAN	Avg.
CLS-pooling w/o pos. enc.	75.5	99.7	99.6	72.2	78.9	98.3	75.6	59.3	82.4
CLS-pooling w/ pos. enc.	85.8	99.0	99.0	83.2	86.7	96.8	88.7	77.8	89.6
Average pooling	88.7	99.8	99.7	74.0	95.7	98.9	80.8	89.7	90.9

B.4 Influence of vision backbone fine-tuning

Our default setup fine-tunes the vision encoder. To quantify the added benefit of this choice, we compare against a variant where we freeze the backbone and train only the LATTE-specific components. Table 9 reports per-generator accuracy for both settings.

Table 9: **Accuracy (%) comparison** for different vision backbones and pooling strategy combinations across generators in the GenImage dataset.

Backbone	Setting	Midjourney	SDv1.4	SDv1.5	ADM	GLIDE	Wukong	VQDM	BigGAN	Avg.
CLIP ViT-L/14	Frozen	60.3	99.8	99.9	53.6	50.3	99.8	51.4	50.1	70.6
	Fine-tuned	98.2	99.9	100	68.4	91.8	99.9	58.9	72.1	86.1
ConvNeXt	Frozen	79.7	99.3	99.1	64.4	74.2	95.9	72.4	70.9	81.9
	Fine-tuned	88.7	99.8	99.7	74.0	95.7	98.9	80.8	89.7	90.9

We observe major improvements for both vision backbones when fine-tuned, with 15.5% accuracy gain for CLIP ViT-L/14 [48] and 9% for ConvNeXt [56]. This likely stems from the fact that frozen backbones retain features that were never explicitly optimized for real vs. fake discrimination, leading to an embedding space that is misaligned with the objectives of generated image detection. Without adaptation, our model may struggle to effectively ground latent trajectories in meaningful visual semantics. Fine-tuning, by contrast, enables the backbone to specialize its representations for this task, enhancing the alignment between visual and latent features essential for robust detection.

B.5 Influence of vision backbones across different processing strategies

In the main paper, we analyze the effect of two different vision backbones - ConvNeXt and CLIP ViT-L/14 - under our default setup (i.e. separate latent processing). In this section, we provide a more comprehensive analysis by exploring how backbone choice interacts with different latent processing strategies - namely, Separate (default), Joint (as introduced in Section A.2) and CLS-based (as described in Section 4.4) - to better understand their combined influence on performance.

Table 10: Detection accuracy (%) for different backbone and pooling strategy combinations across generators in the GenImage dataset.

Config.	Backbone	Midjourney	SDv1.4	SDv1.5	ADM	GLIDE	Wukong	VQDM	BigGAN	Avg.
Separate	CLIP ViT-L/14	98.2	99.9	100	68.4	91.8	99.9	58.9	72.1	86.1
	ConvNeXt	88.7	99.8	99.7	74.0	95.7	98.9	80.8	89.7	90.9
Joint	CLIP ViT-L/14	96.2	100	100	63.4	85.2	99.9	59.2	65.9	83.7
	ConvNeXt	88.4	99.7	99.6	72.5	94.4	98.6	79.4	88.9	90.2
CLS	CLIP ViT-L/14	93.3	99.9	99.9	64.7	85.9	99.4	58.3	63.0	83.0
	ConvNeXt	85.8	99.0	99.0	83.2	86.7	96.8	88.7	77.8	89.6

As shown in Table 10, *Separate latent processing* remains the most effective strategy across both backbones, confirming the value of maintaining timestep-specific representations when modeling the denoising trajectory. Among the configurations, ConvNeXt [56] with Separate pooling achieves the highest overall accuracy (90.9%) and demonstrates stronger generalization to challenging generators like VQDM(80.8%) and BigGAN(89.7%). In contrast, CLIP ViT-L/14, while excelling on in-distribution generators (e.g., SDv1.4, SDv1.5, Wukong >99.9%), sees notable drops on out-of-distribution ones, suggesting a tendency to overfit to the training domain. Overall, the findings indicate that ConvNeXt generalizes more reliably across diverse generative styles, whereas CLIP ViT-L/14 is more prone to overfitting.

C Embedding Space Analysis

To complete our embedding space analysis from Section 4.5, Figure 8 presents t-SNE plots for the three remaining subsets in the GenImage dataset, namely the SDv1.5, Wukong and VQDM generators. As before, the top row shows embeddings extracted with the frozen ConvNeXt backbone (pre-LATTE) and the bottom row shows embeddings after LATTE fine-tuning.

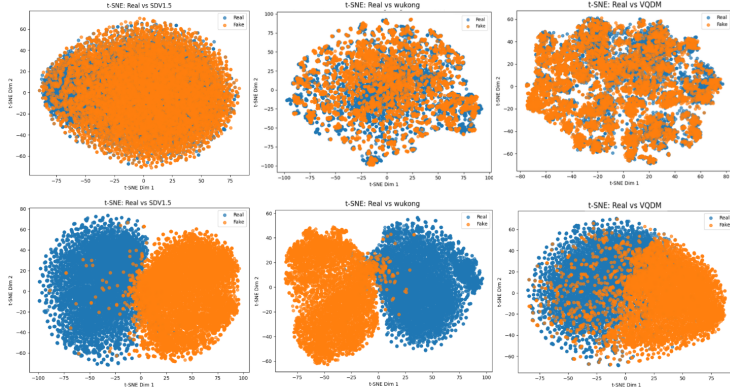


Figure 8: **Visualizations of t-SNE embeddings for real and fake images across the remaining three generators from GenImage.** The first row presents embeddings before using LATTE (extracted using the original ConvNeXt), while the second row shows embeddings derived from LATTE. The reduced overlap in the second row indicates LATTE’s discriminative power and generalization capabilities.

D Latent Trajectory Spatial Analysis

To distinguish how diffusion-based reconstructions differ between real and generated images — and to motivate the modeling the latent trajectory — we analyze the spatial distribution of latent denoising corrections across timesteps.

Specifically, we compute the average per-pixel norm of latent differences between consecutive denoising steps - denoted as $\Delta z_t = |z_t - z_{t-1}|_2$ - for a sequence of tracked timesteps t_1, t_2, \dots, t_K . For each timestep interval $t_{k-1} \rightarrow t_k$, we aggregate Δz_t across all spatial positions and across a batch of samples to obtain a mean spatial correction heatmap:

$$H_{t_k}(x, y) = \mathbb{E}_n \left[\left| z_{t_k}^{(n)}(x, y) - z_{t_{k-1}}^{(n)}(x, y) \right|_2 \right],$$

where (x, y) indexes spatial coordinates and n indexes the samples. The resulting heatmaps visualize how the latent representation evolves across timesteps by capturing the spatial magnitude of change between consecutive steps. They serve as a proxy for identifying where and how strongly the model updates its latent estimated at each stage of the denoising process. This spatial perspective complements our temporal trajectory modeling and helps reveal structural patterns that distinguish real and generated images.

Based on Figure 9, we observe a clear dichotomy between real and fake images across most generators. The real images follow a smooth, uniformly paced denoising trajectory, indicating that each denoising correction is modest in magnitude and spatially consistent.

Fake images, in contrast, break this steady pattern in different ways. Images generated by Glide (9a) require substantially larger corrections overall. The early steps are especially bright - indicating heavier refinement in the beginning of the denoising process - before tapering off into smaller updates. Midjourney (9d) and BigGAN (9e) behave almost identically, with lower differences between real and fake heatmaps than Glide, but still pronounced at every step. Unlike the real’s constant gradual decline, their fake trajectories show a striking front-loaded burst: the jump in Δz between the first two steps is far greater than any subsequent change. This pattern reveals that, for these generators, most of the refinement occurs in the first half of the trajectory, with little correction applied later.

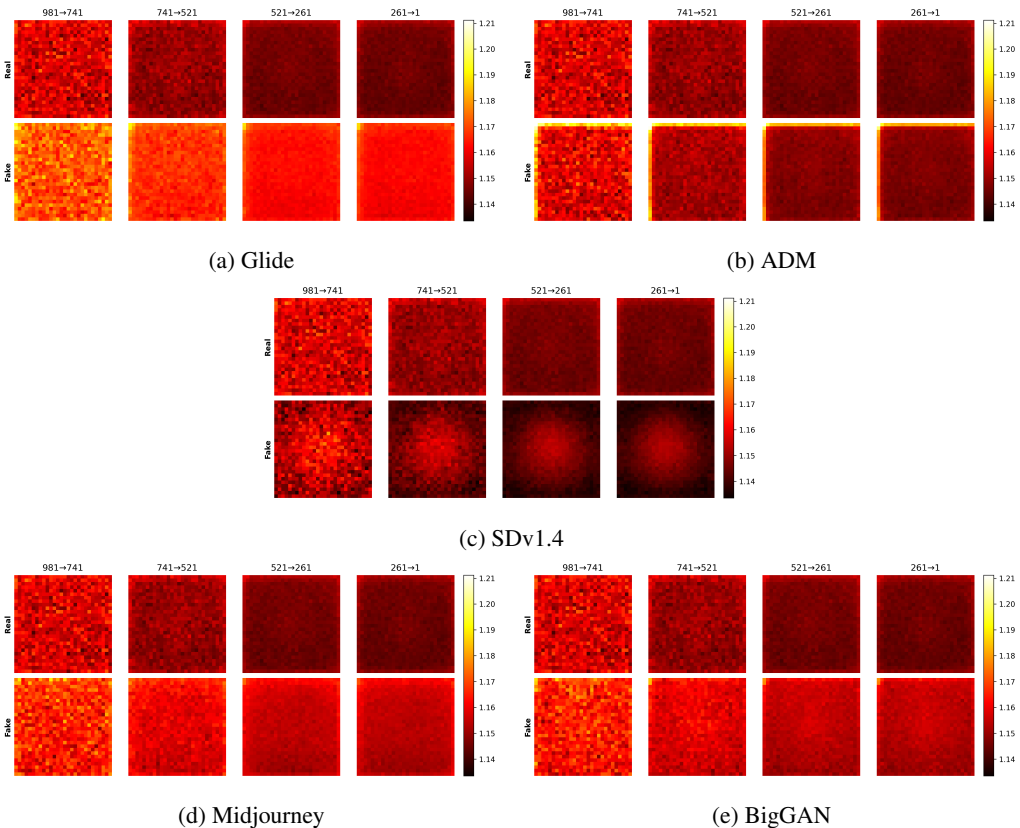


Figure 9: **Latent trajectory spatial analysis using images from the GenImage dataset.** The real images plots represent averages over all real images in the dataset, while the fakes are plotted separately based on the generators used to produce them.

By contrast, the ADM subset (9b) shows a markedly different trend. Here, the real vs. fake differences across all steps are considerably more subtle, and the resulting Δz heatmaps for both classes appear visually similar in both magnitude and spatial pattern, with the exception of small brighter left and top margins. This behavior is consistent with our model’s relatively poor performance on ADM (74% compared to the 90.9% average) and suggests that the images in this subset are particularly difficult to distinguish - even in trajectory space.

Finally, SDv1.4 (9c) presents the most distinctive behavior. Unlike previous generators, the fake heatmaps exhibit a center-focused Δz signature. This effect likely arises because we use Stable Diffusion [7] for both generating and reconstructing the images. The denoiser has learned to prioritize central content - where objects are typically located during prompt-guided generation - and thus applies larger, spatially focused corrections in the center of the image. Real images, by contrast, lack this learned structure and receive relatively uniform and lower-magnitude corrections across space.